Group-contribution coarse-grained molecular simulations of polystyrene melts and polystyrene solutions in alkanes using the SAFT-γ force field

Guadalupe Jiménez-Serratos,[†] Carmelo Herdes,[‡] Andrew J. Haslam,[†] George Jackson,[†] and Erich A. Müller[*,†]

[†]*Department of Chemical Engineering, Imperial College London, London SW7 2AZ, UK*

[‡]*Department of Chemical Engineering, University of Bath, Bath BA2 7AY, UK*

E-mail: e.muller@imperial.ac.uk

Abstract

A coarse-grained (CG) model for atactic polystyrene is presented and studied with classical molecular-dynamics simulations. The interactions between the CG segments are described by Mie potentials, with parameters obtained from a top-down approach using the SAFT-γ methodology. The model is developed by taking a CG model for linear-chain-like backbones with parameters corresponding to those of an alkane model, and decorating it with side branches with parameters from a model of toluene, which incorporate an "aromatic-like" nature. The model is validated by comparison with the properties of monodisperse melts, including the effect of temperature and pressure on density, as well as structural properties (the radius of gyration and end-to-end distance as functions of chain length). The model is employed within large-scale simulations that describe the temperature-composition fluid-phase behaviour of binary mixtures of polystyrene in *n*-hexane and *n*-heptane. A single temperature-independent unlike interaction energy parameter is employed for each solvent to reproduce experimental

solubility behaviour; this is sufficient for the quantitative prediction of both upper and lower critical solution points and the transition to the characteristic "hour-glass" phase behaviour for these systems.

Introduction

As a consequence of its relatively simple chemical structure, polystyrene (PS) has become a ubiquitous model system for fundamental studies aimed at understanding the behaviour of more-complex macromolecules and supramolecular assemblies. From the point of view of molecular simulation, PS is a useful benchmark, as it has been studied with fully atomistic, united-atom, and coarse-grained representations, as well as multiscale approaches. From the considerable literature pertaining to fully atomistic or united-atom works, one can highlight References [1–7] as exemplifying the varied properties and phenomena studied: structure and dynamics; polymer networks and their gas solubilities and diffusivities; stress response; and the elastic behaviour of thin films. In spite of impressive advances in computer power, the computational expense incurred by retaining such a detailed description still limits the system size of the computational cell, which scales exponentially with the molecular weight of the polymer. This becomes relevant as some macroscopic properties such as phase equilibria require particularly large systems to properly explore the several coexisting bulk phases. This difficulty can be alleviated through coarse graining; the atomistic detail and the degrees of freedom of the model are reduced by representing groups of atoms as simple segments or "superatoms", where the interactions are modelled with effective force fields[8]. In the current work we focus on modelling PS melts and PS in solution with alkanes, which correspond to scales of length and time where coarse-grained (CG) models provide an appropriate description.

Coarse graining the polystyrene molecule requires a grouping of the force-field centres in such a way that the intermolecular forces (which characterize the overall energetics) and the shape and morphology (which characterize the entropic contributions of the chain molecules)

are both duly acknowledged. It is ultimately the balance between energy and entropy, *i.e.*, the free energy, that determines the macroscopic thermophysical quantities. It is in this sense that the SAFT coarse-graining modelling approach excels; the overall shape and connectivity of the original molecules is retained while the free energy is faithfully represented through a direct link to an equation of state.

A comprehensive review of recent CG models of PS has been given by Karimi-Varzaneh *et al.*[9]. They summarise the general characteristics of the various CG models, the methodologies used to obtain the force fields, and comparisons of the performance of each model in terms of the representation of a variety of structural and dynamical properties, of melts (both without deformation and under shear) and solutions[10–26]. An outstanding problematic issue with the existing CG models is the lack of representability; the performance of the model deteriorates when it is used for thermodynamic conditions which are different to those pertaining to the states considered in the development of the model parameters (*cf.* the specific examples discussed in References [9,21,25,27]).

In contrast to the CG approaches reviewed in Reference [9], here we adopt the SAFT-γ top-down approach reviewed in Reference [8]. An analytical equation of state (the most recent version[28] of the Statistical Associating Fluid Theory, SAFT[29,30]) is used to develop molecular-force-field parameters from macroscopic thermodynamic information, both for the solvents and the representative molecules used to represent the PS moieties. Under the SAFT-γ description, the molecules are modelled as chains of spherical segments characterized with an isotropic intermolecular potential of the Mie form. While any engineering equation of state (EoS) can be used as a tool for correlating and extrapolating macroscopic thermophysical data, SAFT is one of the very few rigorous molecular-based EoSs that is sufficiently accurate to represent the intermolecular potential on which the corresponding molecular model is based.

A number of versions of the SAFT EoS have been developed, distinguished primarily by the interaction potential employed to describe the intermolecular forces between the

unbonded segments (see, *e.g.*, Reference [31] for a review). In our current work we employ a recently developed group-contribution version, referred to as SAFT-γ Mie or, simply, SAFT-γ[28], which is based on the parent SAFT-VR Mie[32] formulation and employs the Mie potential to represent the inter-segment dispersion interactions. An abridged description of SAFT-VR Mie is presented in References [33, 34]. A unique feature of the analytical expressions contained within both SAFT-VR Mie and SAFT-γ is the accuracy in linking macroscopic thermodynamic properties to the underlying molecular force fields. It follows that SAFT-γ allows a direct link to be made between the experimental thermophysical-property data (*e.g.*, densities, vapour pressures) and the parameters of a force field that corresponds to an effective pair-wise potential exhibiting the same macroscopic behaviour when employed in molecular simulation.

Modelling the phase behaviour of polymer solutions using molecular simulation is a multi-faceted challenge. Models for polymers must be detailed enough to incorporate the correct physics (*i.e.*, connectivity, energetics, etc.) but should not be onerous in terms of computation, and should hence incorporate some degree of coarse graining; obtaining the right balance is the crux of the problem. In our current paper we describe the development of a CG model of PS using SAFT-γ and compare the resulting thermophysical and structural properties with the corresponding properties of higher-fidelity models and real PS, as determined experimentally. The fluid-phase behaviour of solutions of PS in *n*-hexane and *n*-heptane solvents is explored.

Polymer solutions

A characteristic temperature-volume fraction (composition) (T, Φ) phase diagram for polymer solutions[35–37] is provided in Figure 1. The regions highlighted represent liquid-liquid (LL) demixing regions, each bounded by an upper critical solution temperature (UCST) or a lower critical solution temperature (LCST). Typically, if the molecular weight of polymer

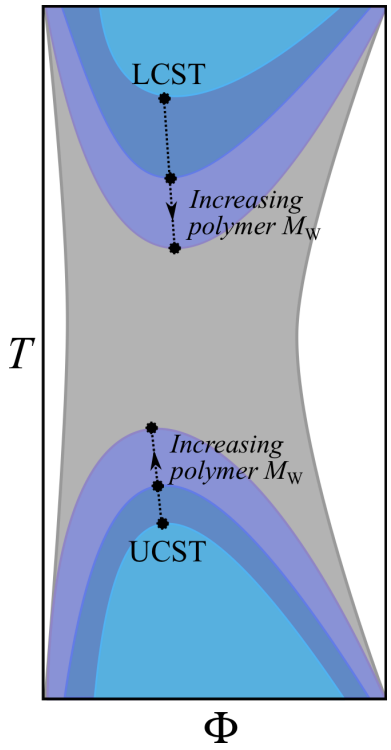

Figure 1: Schematic temperature-volume fraction (composition) (T, Φ) phase diagram for polymer solutions. The darker, blue shaded areas represent liquid-liquid demixing regions for different molecular weights of the polymer, each bounded by upper or lower critical solution temperatures (UCST or LCST indicated by the black circles). The demixing regions become larger with increasing polymer molecular weight; the UCST increases and the LCST decreases (as indicated with the arrows) until both regions merge into an "hour-glass" shaped diagram (represented by the grey shading). (Coloured on-line version.)

is increased, the UCST tends to rise and the LCST tends to lower; for higher molecular weights. both regions can merge to form a so-called "hour-glass" demixing diagram. The appearance of the LCST in the higher-temperature region is well understood as an effect due to the compressibility of the solution at such conditions. References [35–38] offer a deeper discussion of polymer-solvent diagrams. Here, we use the SAFT-γ CG models for PS and solvents to explore this type of fluid-phase behaviour via molecular-dynamics (MD) simulation. We note in passing that it is not appropriate to use the SAFT-γ Mie EoS to calculate the phase diagrams for branched chains since the details of structure and connectivity of the polymer are not explicitly taken into account.

The experimental values of the UCST and LCST for the systems of interest[35,39] are summarised in Table 1; the experiments were carried out for volume fractions of polymer between 0 and 0.4 in the case of polymers with a narrow molecular-weight distribution ($M_{\mathrm{w}}/M_{\mathrm{n}} < 1.06$, where M_{n} is the number-average molecular weight). We adopt the nomenclature "PSx" to refer to polystyrene with a molecular weight of x g mol^{-1}. The fluid-phase behaviour of solutions of PS4800 in n-hexane is characterized by an "hour-glass" diagram, wherein demixing appears in the interval ($0.07 \leq \Phi \leq 0.32$) for all temperatures[39]. The other systems exhibit upper and lower demixing regions, bounded by the two critical temperatures given in Table 1.

Table 1: Experimental[35,39] upper and lower critical solution temperatures for PS + n-hexane and PS + n-heptane.

System	UCST / K	LCST / K
PS2030 + n-hexane	318	470
PS4800 + n-hexane	–	–
PS2030 + n-heptane	311	515
PS4800 + n-heptane	359	477

Models

The molecular models adopted here are coarse-grained chains of tangent spherical segments, interacting via a Mie potential. We use the SAFT-γ Mie EoS[28,32] to obtain the inter-segment potential parameters relating to the CG segments. Each molecule is represented by n spherically symmetrical segments characterized by a size σ, closely related to an average diameter. We model the inter-segment interactions with a particular case $(\lambda, 6)$ of the Mie potential:

$$u(r) = \mathcal{C}\epsilon \left[\left(\frac{\sigma}{r}\right)^{\lambda} - \left(\frac{\sigma}{r}\right)^{6} \right], \tag{1}$$

where r is the distance between centres of a pair of segments, ϵ is the depth of the potential-energy well, λ is the repulsive exponent and $\mathcal{C}$ is a constant defined (for the $(\lambda, 6)$ Mie) as

$$\mathcal{C} = \frac{\lambda}{\lambda - 6} \left(\frac{\lambda}{6}\right)^{\frac{6}{\lambda - 6}}. \tag{2}$$

The adoption of the particular Mie $(\lambda, 6)$ form (in preference to the more generic $(\lambda_{\mathrm{r}}, \lambda_{\mathrm{a}})$ form) follows from the demonstration[40] that, for the description of fluid-phase behaviour, the repulsive and attractive exponents are not completely independent; this inter-relationship reduces the degrees of freedom, thereby allowing the attractive exponent to be fixed to the London-dispersion[41] value of six. The potential parameters, σ, ϵ and λ, are obtained in one of two ways, depending on the availability of suitable experimental data. In the first instance, the parameters are estimated in order to best represent the experimental vapour-liquid phase-equilibrium data, as described in References [8] and [42]. Alternatively, the parameters can be determined in expedited fashion from corresponding-states correlations, linking them to the experimental acentric factor, critical temperature, and liquid density, respectively; the details of the latter methodology are given in References [43], [44] and [45].

Solvents

Two alkane solvents are examined in our current study: n-hexane and n-heptane. The solvents are modelled as homonuclear chains comprising $n = 2$ segments, with each segment chosen to represent a group of three to four carbon backbone atoms. The inter-segment parameters are obtained following the procedure set out in References [43] and [44] and are given in Table 2. The same set of parameters is used for the SAFT-γ theoretical phase diagrams as for the MD simulations presented in the *Results* Section.

Table 2: SAFT-γ Mie force fields for the model CG segments studied in our work: unlike interaction parameters, k_{ij}, segment diameter, σ; energy well depth, ϵ (after applying the corresponding k_{ij} parameter); and the repulsive Mie exponent, λ, respectively. The polymer and solvent molecules are constructed from these building blocks as described in the text.

	k_{ij}	σ/Å	$(\epsilon/k_{\mathrm{B}})$/K	λ
Solvents				
n-hexane	–	4.515	379.07	19.57
n-heptane	–	4.766	436.87	23.91
Polystyrene				
backbone (alkyl)	–	4.180	377.14	16.43
branch (aromatic)	–	4.260	410.27	16.83
Unlike interactions				
backbone-branch	0.000	4.220	393.30	16.63
backbone-hexane	-0.010	4.348	381.04	17.92
branch-hexane	0.055	4.388	372.20	18.14
backbone-heptane	-0.010	4.473	407.33	19.76
branch-heptane	0.045	4.513	402.41	20.01

Polystyrene

In group-contribution approaches one can exploit the transferability of CG models for small molecules or chemical functional groups of atoms in the development of models of larger or more-complicated molecules[28,46,47]; this lies at the heart of the CG philosophy. The SAFT-γ methodology has already been successfully applied in this way to represent the phase equilibria and structure of linear polymers and surfactants[48–51]. Conversely, a large molecule can be

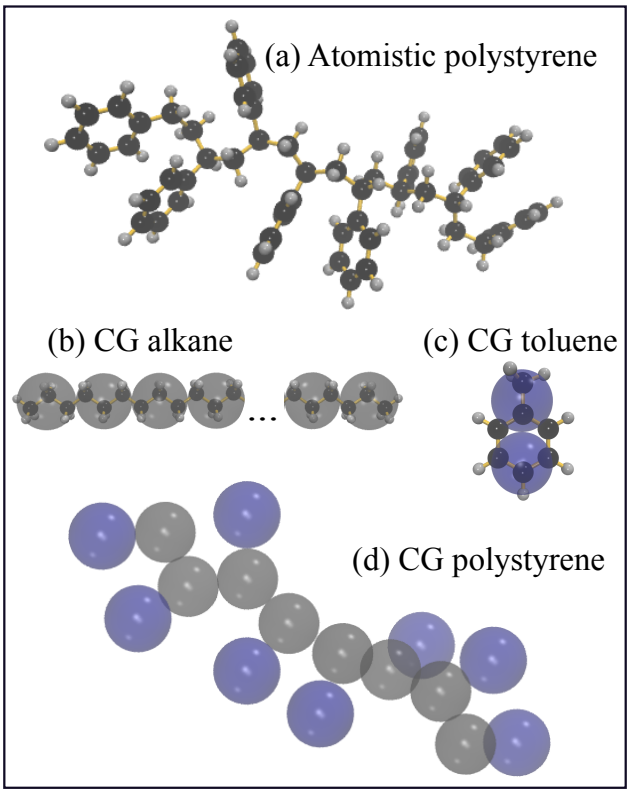

Figure 2: (a) Atomistic representation of polystyrene. To use a group-contribution coarse graining, we visualize the polymer as an aliphatic backbone with aromatic branches. (b)–(d) Representation of the group-contribution approach used to build the polystyrene CG model. The building blocks are segments of a CG alkane and segments of a dimer model of the toluene molecule. The resulting CG model for polystyrene is an alkane-like backbone with aromatic moieties comprising one half of the toluene model. (Coloured on-line version.)

subdivided into functional groups chosen to simplify the coarse graining; this is the approach taken here to build our polystyrene CG model. The procedure is summarized schematically in Figure 2. The atomistic polystyrene chain can be seen as an aliphatic backbone decorated with aromatic branches. Our CG "backbone" is a long alkane with parameters estimated the using SAFT-γ Mie methodology using target experimental vapour-liquid equilibria data relating to n-C_9H_{20}, n-$C_{12}H_{26}$, and n-$C_{15}H_{20}$, as presented in Reference [48]. The original alkane model comprised two types of segments: "end" segments, representing CH_3–CH_2–CH_2–, and "middle" segments, representing –CH_2–CH_2–CH_2–; intramolecular interactions (bonds and angular restrictions) derived from fitting distribution functions obtained from atomistic simulations were also included. For the sake of simplicity, we reduce the backbone to a homonuclear chain of "middle" segments (Figure 2 (b) and (d)) and omit the intramolecular restrictions, resulting in a fully flexible chain of tangent segments. The "backbone" alkyl-chain parameters are given in Table 2.

The moiety used to represent the aromatic branches is half (one segment) of our (dimer) model of a toluene molecule, as shown in Figure 2 (c) and (d); the molecular parameters for this toluene model are obtained following Reference [43], and correspond to those of the "branch" aromatic moiety given in Table 2.

In summary, the monomer (repeat unit) of our PS model is represented by two segments, one aliphatic in nature and another aromatic in nature, thereby accounting for the more important physical features required for a model at this level of coarse graining. In comparison to fused models, tangential models effectively include more carbons per monomer than is implied by the original molecule or atomic grouping on which the CG model was based (*cf.* the discussion in Reference [47]). This is accounted for insofar as the segments of our model represent 3 carbons for the aliphatic segment and 3.5 carbons for the aromatic segment, tallying to 6.5 carbons per monomer; in comparison, there are a total of 8 carbons in the monomer of an actual PS molecule. This apparently odd choice of attaching only half a toluene molecule to every three backbone carbons (represented by a backbone

segment) should not be taken literally: top-down CG models do not necessarily reproduce the atomistic detail, but incorporate information about the effective average interactions and general shape and connectivity of the molecule. We also note that in our model the aromatic branches are, in effect, randomly oriented in relation to the backbone, whereby the model best represents an atactic PS molecule. The parameters relating to the inter-segment potentials for the PS model are given in Table 2.

Unlike interactions for mixtures

The combining rules used to represent the cross interactions between unlike segments i and j are

$$\sigma_{ij} = \frac{\sigma_{ii} + \sigma_{jj}}{2} \tag{3}$$

(the Lorentz rule) for the diameters,

$$\lambda_{ij} - 3 = [(\lambda_{ii} - 3)(\lambda_{jj} - 3)]^{1/2} \tag{4}$$

for the repulsive exponent[32], and

$$\epsilon_{ij} = (1 - k_{ij}) \frac{\sqrt{\sigma_{ii}^3 \sigma_{jj}^3}}{\sigma_{ij}^3} \sqrt{\epsilon_i \epsilon_j} \tag{5}$$

(Berthelot-like rule) for the energy[32], where the adjustable binary-interaction parameter, k_{ij}, is kept as zero unless otherwise stated.

Reliable CG models for pure systems do not necessarily lead to a good description of their mixtures, since the standard combining rules (with $k_{ij} = 0$) correspond to mathematical averages that strictly speaking have a sound physical justification only for simple, small, near-spherical molecules that interact only through London dispersion interactions[52]. For more-complicated molecules, such as those considered in our current study, the adjustment of the binary-interaction parameter k_{ij} in Equation 5 allows one to account for

this extra complexity, providing ultimately for a better description of their experimental behaviour. Following the SAFT-γ methodology, the estimation of binary-interaction parameters is typically carried out by minimizing an objective function constructed as the difference between an EoS prediction and experimental information related to fluid-phase equilibria, *e.g.*, isothermal pressure-composition or isobaric temperature-composition data, or to other thermodynamic properties such as volumes of mixing[37,53–56]. However, in the SAFT theory we employ it is implicit that the chains representing the molecules are linear. In this sense, there is a clear mismatch between the theory and the simulations so that this procedure is not directly appropriate for our current study. Rather, any required adjustment to the k_{ij} values can be judged only from the MD simulations themselves.

In our simulations two unlike interactions between PS and the solvent (n-hexane or n-heptane) are included: backbone-solvent $k_{\mathrm{bbn-sol}}$, and branch-solvent $k_{\mathrm{bch-sol}}$. In practical terms, obtaining both of the corresponding binary-interaction parameters simply by adjusting the MD simulation data to capture the experimental behaviour would be prohibitively time-consuming. However, the influence of these two parameters is partially coupled and one would expect some degeneracy insofar as different combinations of these two parameters will lead to essentially the same behaviour. We therefore assign a value to one unlike-interaction parameter, and just adjust the other. The backbone should feature an affinity to aliphatic solvents; to accentuate this affinity we assign a small negative value, $k_{\mathrm{bbn-sol}} = -0.01$, for the backbone-solvent interaction in all our systems. The remaining unlike-interaction parameter, $k_{\mathrm{bch-sol}}$, is adjusted directly in the simulations. In order to bound the $k_{\mathrm{bch-sol}}$ value for each solvent, simulations are carried out at two key temperatures: one at which immiscibility is expected, to obtain the lower-bound of $k_{\mathrm{bch-sol}}$, and one where full miscibility is the target; the upper bound is identified as the maximum value of $k_{\mathrm{bch-sol}}$ that fulfills this condition. A third simulation at another temperature is used where necessary. The fluid-phase behaviour of the mixture is characterized using histograms of the local compositions; these are discussed further in the *Results* section.

The branch-solvent unlike-interaction parameters used in our current work are $k_{\mathrm{bch-sol}} = 0.055$ when the solvent is n-hexane and $k_{\mathrm{bch-sol}} = 0.045$ when the solvent is n-heptane. The unlike potential parameters are summarised in Table 2. We emphasize that the unlike-interaction parameters for both solvents are obtained using the PS2030 systems and transferred without further modification to the PS4800 systems for use over a wide range of temperatures and compositions.

Simulation details

Three types of systems are simulated: pure solvents; PS melts; and PS solutions. All of the MD simulations are performed using HOOMD-blue[57–59] on single NVIDIA Tesla K40 GPUs. The fluid-phase equilibria and single-phase systems are studied under canonical (NVT) and/or isobaric-isothermal (NPT) conditions. Neighbouring segments on the same chain interact with each other only through a harmonic-spring potential characterized by the spring constant k_{H}; segments separated by more than one bond interact via a Mie potential, as described earlier. In this way our model retains a link with the SAFT description. The spring constant, relating to the bond between linked segments, is set to $k_{\mathrm{H}} = 20000$ kJ mol^{-1} nm^{-2}. The time step is $\Delta t = 0.01$ ps in all cases and the cut-off distance is set to 28 Å. The NVT simulation is accomplished using the Martyna-Tobias-Klein (MTK) integration of the equations of motion[60,61] based on the Nosé-Hoover thermostat[62,63], while the NPT simulation is performed using the MTK barostat-thermostat[60,64,65]. Solvents systems with $N_{\mathrm{mol}} = 5000$ molecules ($N_{\mathrm{tot}} = 10000$ segments) are simulated over $t = 80$ ns corresponding to wall-clock times between 7 and 14 hours. The most computationally demanding simulations are the mixtures, with around $N_{\mathrm{tot}} \approx 10^5$ segments. Some of these systems require $t = 400$ ns of simulation time, corresponding to 800 hours of wall-clock time. Specific details for each type of system are given in the *Supporting Information*.

Results

Solvents

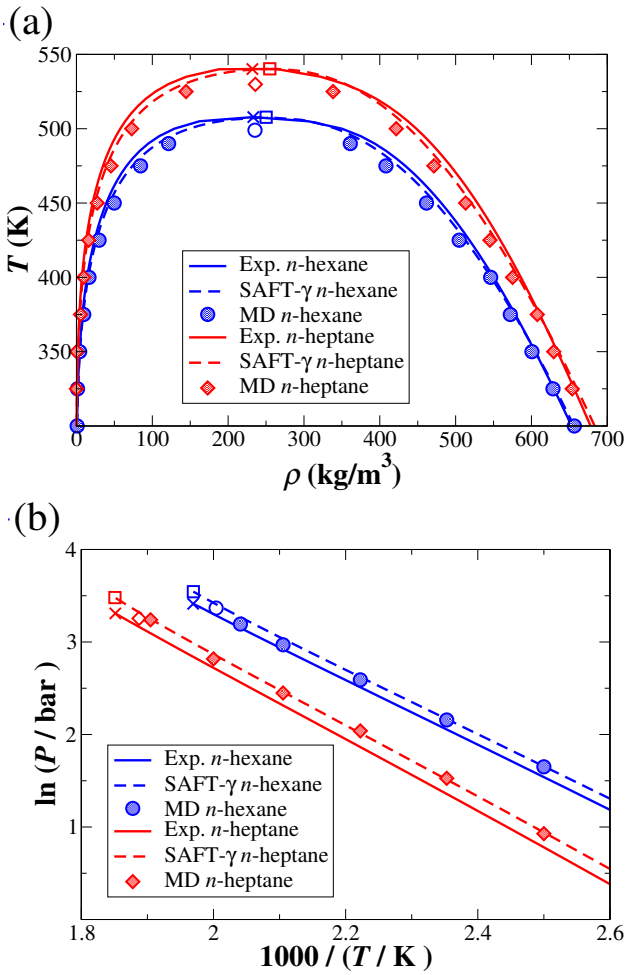

Figure 3: (a) Vapour-liquid coexistence curves and (b) vapour-pressure curves of the fluid-phase equilibria for pure n-hexane and pure n-heptane. The smoothed experimental data (continuous curves) are taken from NIST[66,67]; the crosses indicate the experimental critical points. The dashed curves represent the theoretical description given by the SAFT-γ EoS; the critical points are indicated by the open squares. The filled symbols represent the MD results obtained from direct coexistence NVT simulations (error bars are of the order of the symbol sizes and are not shown), while matching open symbols indicate the corresponding critical points. (Coloured on-line version.)

Direct coexistence NVT simulations and single-phase NPT simulations of pure systems are performed to establish a benchmark. There are advantages in the use of direct coexistence simulations over Gibbs ensemble Monte Carlo (GEMC) methods in studies of fluid-

phase equilibria[68,69]. Although the explicit inclusion of an interface inevitably requires the use of relatively large system sizes, conventional computational capabilities are sufficient in the case of the system under study here. The use of direct coexistence methods circumvents issues associated with insertion (and deletion) of large particles at liquid-like densities required to achieve equilibrium states through GEMC simulations. In Figure 3 we present the vapour-liquid coexistence envelopes and the vapour-pressure curves obtained for the fluid-phase equilibria of *n*-hexane and *n*-heptane by MD simulations. For comparison, we include the smoothed experimental information obtained from NIST[66,67] as well as SAFT-γ[28] EoS calculations, using the same models (Table 2) as in the MD simulations. The average simulated values are obtained using the analysis tools from GROMACS[70]. A good correspondence between theory, simulation and experiment is apparent from both plots, although the quality of the descriptions from both the theory and simulation is better in terms of the saturation densities (Figure 3(a)) than the vapour pressures (Figure 3(b)), where small deviations of both the theory and simulation from experiment can be seen at higher temperatures.

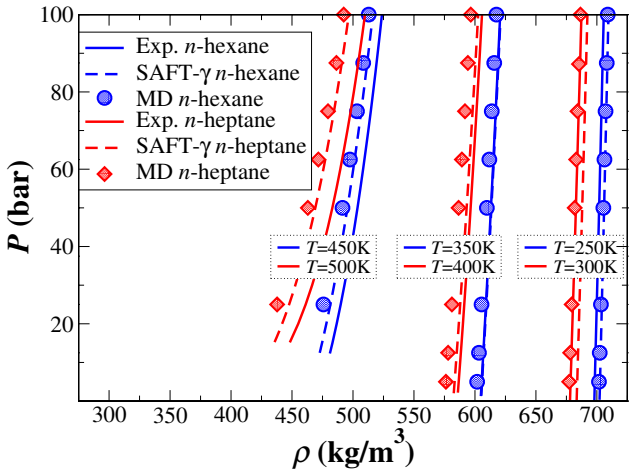

Figure 4: Pressure-density (P-ρ) isotherms for systems of pure *n*-hexane and pure *n*-heptane. Symbols as in Figure 3. (Coloured on-line version.)

To test the compressibility of the CG models in the liquid region, NPT simulations of single-phase systems are performed. Three isotherms are tested for each system starting from pressures close to the corresponding saturation value up to 100 bar. The densities

obtained after equilibration are plotted in Figure 4, where the corresponding NIST data[66,67] and SAFT-γ calculations are included for comparison. A good correspondence is observed between all of the data sets, with a slight deterioration for the higher-temperature isotherms, which is expected due to the proximity to the critical region.

Polystyrene melts

Table 3: Simulation details and results for the PS melts at a temperature of $T = 500$ K and pressure of $P = 1$ bar. N_{mono} represents the number of styrene units per chain; N_{chain} is the number of chains, and ρ represents the equilibrium densities obtained in the NPT simulations. $\langle R \rangle$ and $\langle R_{\text{g}} \rangle$ correspond to the ensemble averages of the end-to-end distance and radius of gyration (respectively), obtained from NVT simulations.

N_{mono}	N_{chain}	ρ / (kg/m^3)	$\langle R \rangle$ / Å	$\langle R_{\text{g}} \rangle$ / Å
10	500	900.5 ± 3.3	15.8 ± 0.2	6.16 ± 0.04
20	500	909.6 ± 2.3	24.0 ± 0.3	9.41 ± 0.07
30	500	912.3 ± 2.0	30.2 ± 0.6	11.9 ± 0.1
50	400	914.9 ± 1.7	40.0 ± 0.9	15.8 ± 0.1
100	400	916.8 ± 1.1	57.7 ± 0.7	22.9 ± 0.1
150	300	917.4 ± 1.0	69.6 ± 0.7	27.8 ± 0.2
200	300	917.6 ± 0.9	81.3 ± 0.7	32.2 ± 0.1
250	250	917.9 ± 1.0	88.3 ± 1.0	35.0 ± 0.1
300	200	917.8 ± 0.9	94.8 ± 1.1	39.0 ± 0.2
300	500	918.0 ± 0.6	95.8 ± 0.8	39.03 ± 0.06

To test the structural properties of the PS model, monodisperse systems of PS melts corresponding to different chain lengths are simulated, as detailed in Table 3. The equilibrium density is first obtained from the NPT simulations using a molar mass for the styrene unit of $M_{\text{w}} = 104.15$ g/mol. Our results vary from 900 to 918 kg/m^3 for systems with $10 \leq N_{\text{mono}} \leq 300$, where N_{mono} refers to a monomeric moiety, composed in this case of a dimer of a backbone CG segment and a branch CG segment. The density slightly increases with increasing chain length, in agreement with the trend reported in the literature[10,17,24]. The reported experimental density[15,71] for the 10-mer melt is 895 kg/m^3, while a density of $\rho \sim 960$ kg/m^3 was determined Karimi-Varzaneh *et al.*[9] for fully atomistic 10-mers, at sim-

ilar conditions. Once the NPT simulations are equilibrated, NVT simulations are carried out to obtain the ensemble average end-to-end distances $\langle R \rangle$ (calculated from the initial and final backbone segments), and radii of gyration $\langle R_g \rangle$; these are also reported in Table 3. As a test of the system size, the box with the larger polymer, $N_{\text{mono}} = 300$, is simulated with $N_{\text{chain}} = 200$ and $N_{\text{chain}} = 500$ polymer molecules. The averages obtained for both systems are found to differ by less than 1%.

Plots of end-to-end distances and radii of gyration as a function of the chain length of the polymer are presented in Figures 5 and 6 together, with values for other CG models taken from the literature for comparison. The structural results for our CG polystyrene are quantitatively similar to those obtained for other CG models, following the same expected trend as the length of the chains is increased.

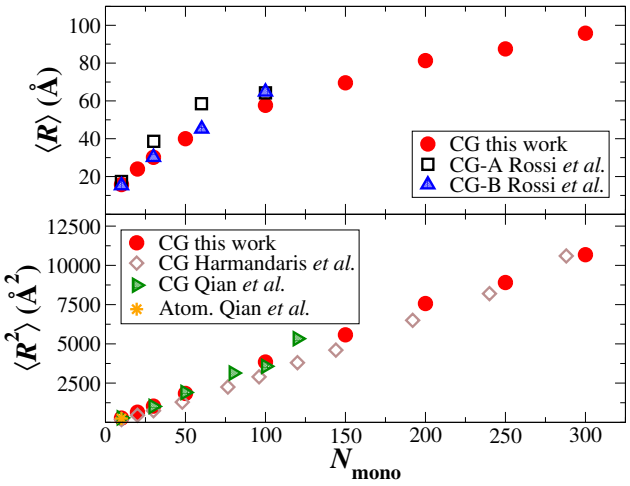

Figure 5: Structural properties for polystyrene melts at a temperature of $T = 500$ K. The ensemble average of the end-to-end distance $\langle R \rangle$ (upper panel), and the mean-square end-to-end distance $\langle R^2 \rangle$ (lower panel) are given as functions of the chain length, represented as the number of monomers N_{mono}. Simulation results for CG polystyrene obtained in our current work are compared with the values of $\langle R \rangle$ obtained by Rossi *et al.*[15] for two CG models, with the values of $\langle R^2 \rangle$ presented by Harmandaris and Kremer[17] for a CG model studied at $T = 463$ K, and with those presented by Qian *et al.*[20]; in the comparison are the values of $\langle R^2 \rangle$ for the atomistic (non-CG) system with $N_{\text{mono}} = 10$, taken from Reference [20].

The Flory characteristic ratio is given by $C_N = \langle R^2 \rangle / N_C l^2$, where l is the atomistic backbone length and N_C is the number of carbon-carbon bonds in the backbone. We calculate C_N taking the atomistic value $l = 1.53$ Å and $N_C \approx 2N_{\text{mono}}$; the results are shown in Figure

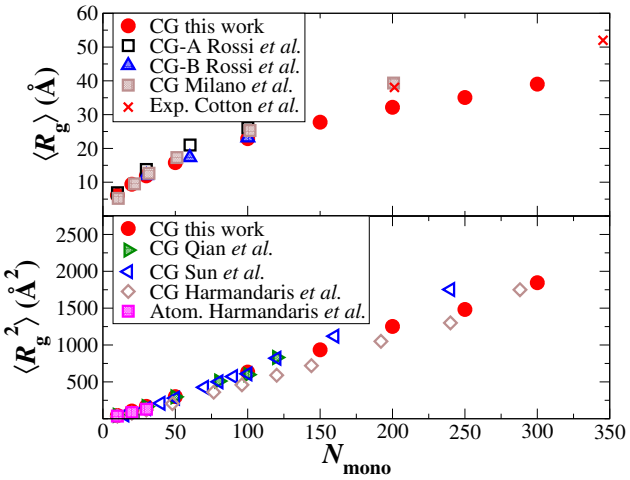

Figure 6: Structural properties for polystyrene melts at $T = 500$ K. The ensemble average of the radius of gyration $\langle R_{\mathrm{g}} \rangle$ (upper panel) and the mean-square radius of gyration $\langle R_{\mathrm{g}}^2 \rangle$ (lower panel), are given as functions of the chain length, represented as the number of monomers N_{mono}. Simulation results for CG polystyrene obtained in our current work are compared with the values of $\langle R_{\mathrm{g}} \rangle$ obtained by Rossi *et al.*[15] for two CG models, with the values of $\langle R_{\mathrm{g}} \rangle$ of Milano *et al.*[10], and also with two experimental $\langle R_{\mathrm{g}} \rangle$ values[10,72] for a PS melt obtained using SANS. Our values of $\langle R_{\mathrm{g}}^2 \rangle$ are compared with those presented by Qian *et al.*[20], with values for the CG model of Sun and Faller[11] at $T = 450$ K, and with the values presented by Harmandaris and Kremer[17] for a CG model studied at $T = 463$ K, as well as their atomistic results presented in Reference [16].

7 and compared with other values reported in the literature. The data taken from Milano *et al.*[10] correspond to simulations at $T = 500$ K, the same temperature as our own simulations, whereas the CG model of Harmandaris *et al.*[16,17] was studied at $T = 463$ K, and the CG model of Hsu *et al.*[21] at $T = 450$ K. The experimental values for the infinite chain are $C_\infty = 8.3$, 8.5, and 8.6,[73,74] respectively. In Figure 7, a dashed line indicates the expected value of $C_\infty = 8.3$ at $T = 500$ K. As can be observed, the characteristic ratio for our model reaches an asymptotic value ~ 8 for systems with $N_{\text{mono}} > 200$.

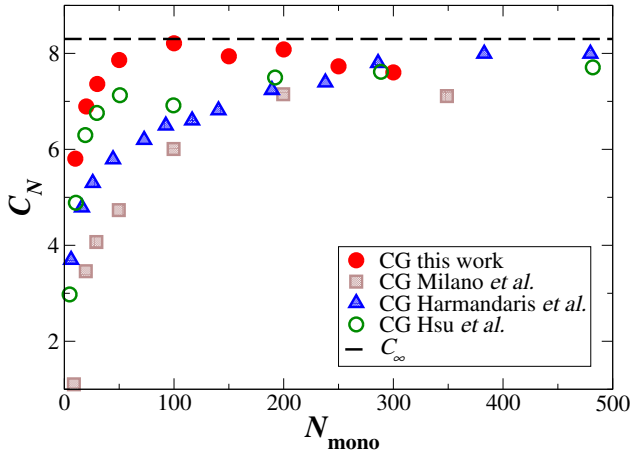

Figure 7: The Flory characteristic ratio, C_N. The black dashed line indicates the experimental value $C_\infty = 8.3$[73,74] at $T = 500$ K. The results of our current work are compared with the values for CG models presented by Milano *et al.*[10], Harmandaris and Kremer[17], and Hsu *et al.*[21].

The flexibility of our model is tested by calculating the angular distribution of the angles formed by three consecutive backbone segments, by backbone-bakcbone-branch tetrads, as well as for the dihedral angle, defined by branch-backbone-backbone-branch tetrads. The systems with the shortest and the largest chains ($N_{\text{mono}} = 10$ and $N_{\text{mono}} = 300$) are tested, resulting in virtually the same distributions. The results for the $N_{\text{mono}} = 300$ system simulated at $T = 500$ K are shown in Figure 8. The angular distribution for the backbone ranges from 60° to 180°, presenting two peaks, one at 67° and a second peak at 115°. These values are considerably smaller than those for CG models with similar structure and connectivity, reported in References [21, 22, 25], where a bimodal distribution with peaks at $\sim 125°$ and

170° was obtained from atomistic simulations and used to adjust the bonded interactions of their CG models. A similar trend is observed for the bbn-bbn-bch angular distribution. The dihedral distribution for our model presents all possible angles with the same probability, while a peak at $\sim 105°$ is reported by Hsu *et al.* for their atactic PS CG model. Our top-down model does not include angular restrictions, which explains the small angles explored by the backbone and the lack of structure in the dihedral distribution. In summary, our model is not developed to resolve the tacticity of PS molecules and is appropriate for the representation of atactic PS. The end-to-end distances and radii of gyration, described earlier in the section, are similar to other CG models in the literature. The agreement of the structural properties at one scale but not at the other could be related to the chain flexibility but also to the bulky representation of the backbone segments.

To evaluate the dynamic behaviour of the PS model, the self-diffusion coefficients for the centres of mass (CM) are calculated as

$$D = \lim_{t\to\infty} \frac{\left\langle \left(\mathbf{R}_{\mathrm{CM}}(t) - \mathbf{R}_{\mathrm{CM}}(0)\right)^2 \right\rangle}{6t}, \tag{6}$$

using simulation trajectories of the melt systems described in Table 3. The CM self-diffusion coefficients as a function of the chain length N_{mono} are shown in Figure 9. The values of the diffusion coefficient are of the order of 10^{-6} cm^2/s for the $N_{\mathrm{mono}} = 10$ system and of 10^{-8} cm^2/s for the $N_{\mathrm{mono}} = 300$ system. These values are between two and three orders of magnitude higher than the experimental values, according to References [75–78]. This factor in the time scaling is typical in CG models, where the reduction of friction due to the coarse representation allows faster dynamics. Regarding the scaling with N_{mono}, we observe a single trend in the diffusion. Correlating the data to a power-law function, $D \sim N_{\mathrm{mono}}^{a}$, gives an exponent $a = 1.23 \pm 0.02$, which is closer to the Rouse model (where $a = 1$) than to the reptation behaviour, which is characterized by an exponent of $a \sim 2$, which is expected for the long-chain systems. This type of two-regime behaviour has been exhibited with other

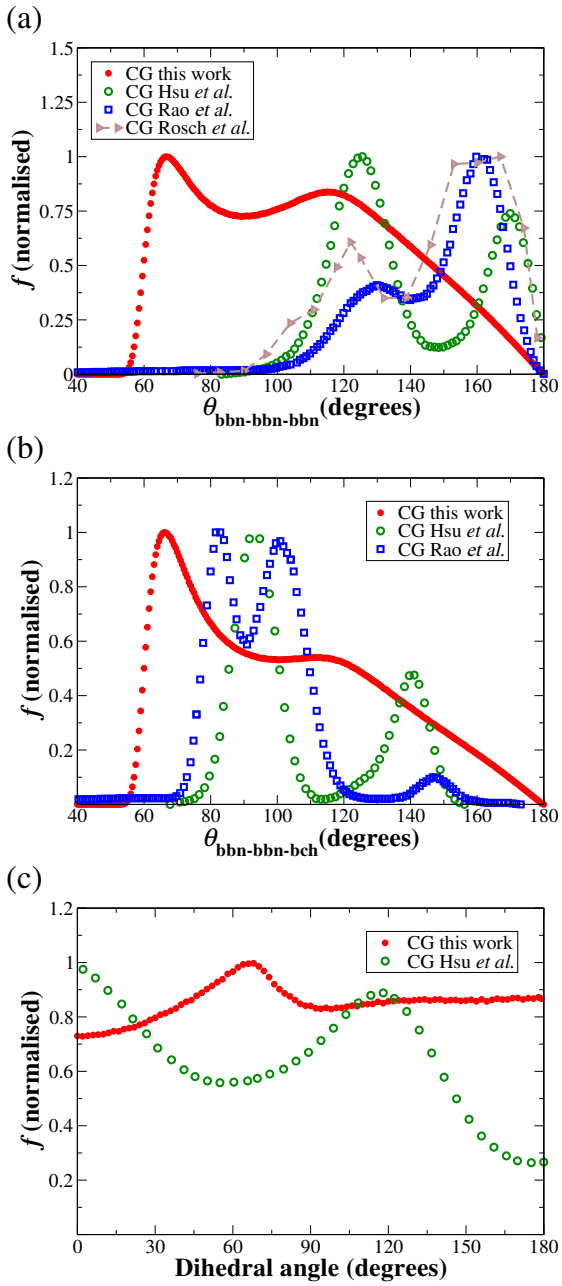

Figure 8: Angular distribution functions for (a) the backbone angle, defined as the angle formed by consecutive bbn-bbn-bbn triads; (b) the backbone-branch angle, defined as the angle formed by consecutive bbn-bbn-bch triads; and (c) the dihedral angle, defined as the angle between the projections of consecutive bbn-bch pairs on the plane perpendicular to the connecting bbn-bbn diad. Our distributions are obtained from the PS system with $N_{\text{chains}} = 500$ polymers of $N_{\text{mono}} = 300$ styrene units simulated at $T = 500$ K. For comparison, we include the corresponding results from CG models with similar structure and connectivity: Hsu *et al.*[21] CG model simulated at a temperature of $T = 300$ K, Rao *et al.*[22] CG model for chains with 40 monomers at a temperature of $T = 300$ K, and Rosch *et al.*[25] CG ("locally shifted higher resolution") model at a temperature of $T = 500$ K. All cases are normalised respect to the corresponding highest peak.

models, for example, those in References [10, 15, 17]. Further understanding of dynamic properties is beyond the scope of our current work; a detailed study of these properties for a CG polystyrene model is discussed by Harmandaris and Kremer in Reference [17].

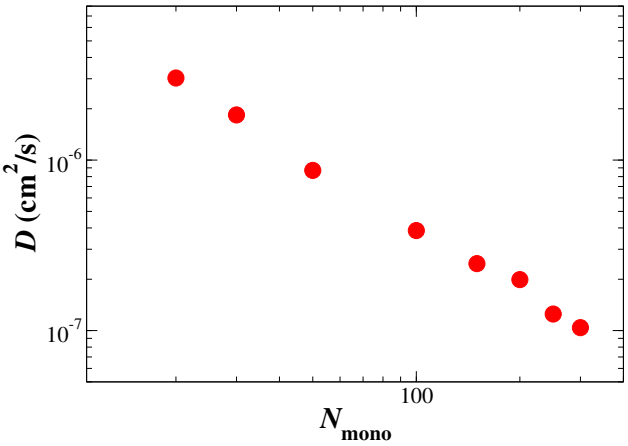

Figure 9: Self-diffusion coefficients as a function of the styrene units N_{mono} in the model of polystyrene. The coefficients are calculated from the displacement of the centres of mass of the chains.

To study the effect of the temperature on the melt density, systems with $N_{\text{mono}} = 10$ are tested under NPT conditions at $P = 1$ bar. In Figure 10 we present the resulting densities as a function of temperature including data for other models in the literature. We note that the CG model of Hsu *et al.*[21] features a variable diameter, which was adjusted as a function of temperature in order to reproduce the experimentally observed density. Problems relating to the representability of the CG models are evident with the CG model of Carbone *et al.*[27]; the temperature dependence of the density follows an incorrect trend, matching the full-atom density (also shown) only at $T = 500$ K, the temperature used to develop the model[27]. Our model leads to densities of the order of the expected values; although the trend with temperature is correct, the slope of our data is seen to be larger than that of the other models. As a result, the thermal expansion coefficient $\alpha = V^{-1} (\partial V/\partial T)_P$ for our system is $\alpha = 10.4 \times 10^{-4}$ K^{-1} at $T = 300$ K, while Hsu *et al.* report $\alpha = 5.50 \times 10^{-4}$ K^{-1} and $\alpha = 5.94 \times 10^{-4}$ K^{-1} for the experimental and fully atomistic simulation values, respectively, at the same temperature.

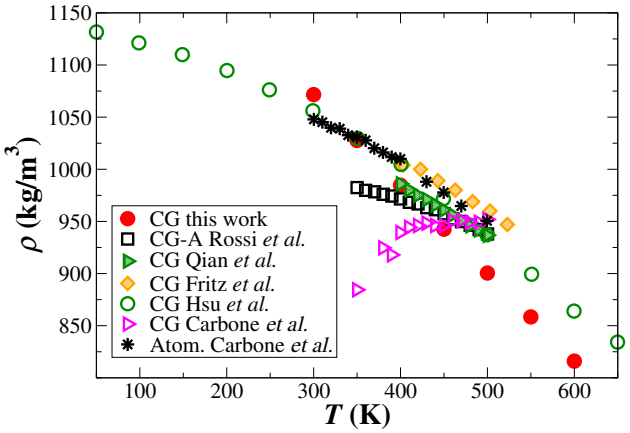

Figure 10: Density as a function of temperature for polystyrene melts with $N_{\mathrm{mono}} = 10$ at $P = 1$ bar. Simulation results obtained with our CG polystyrene model are compared with the results of Rossi *et al.*[15], Qian *et al.*[20], Fritz *et al.*[19] (in agreement with their atomistic simulations, not shown), Hsu *et al.*[21], Carbone *et al.*[27], both for their CG and atomistic models. Note that in the CG model of Hsu *et al.*[21], one of the diameters in the model is adjusted as a function of temperature to achieve density representability.

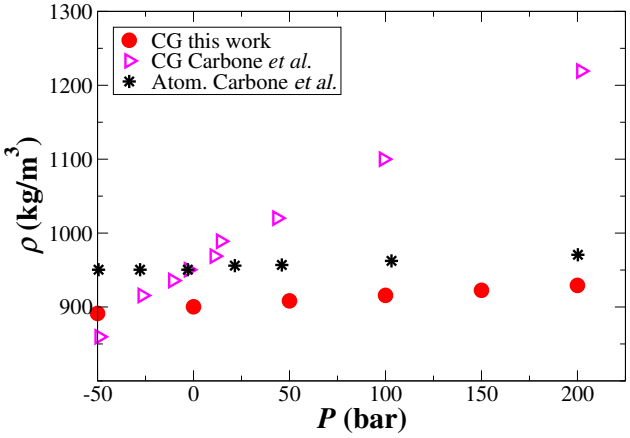

Figure 11: Density as a function of pressure for polystyrene melts with $N_{\mathrm{mono}} = 10$ at $T = 500$ K. Simulation results obtained with our CG polystyrene model are compared with those of Carbone *et al.*[27] for their CG and atomistic models.

We perform further simulations under NPT conditions to test the effect of pressure, where now the temperature is fixed at a value of $T = 500$ K. The resulting densities are shown in Figure 11 as a function of pressure, together with CG and atomistic simulation results of Carbone *et al.*[27] at the same conditions. There are again issues of representability with the model by Carbone *et al.*; the full-atom density is reproduced only at the pressure of $P = 1$ atm, which used to develop the model[27]. In this test, our model gives densities of the order of the expected values and the density-pressure curve has a small slope indicating a high incompressibility. The isothermal compressibility $K_T = V^{-1} (\partial V/\partial P)_T$ for our system is $K_T = 1.64 \times 10^{-6}$ kPa^{-1}, while Carbone *et al.* report $K_T = 9.3 \times 10^{-7}$ kPa^{-1} and $K_T = 1.6 \times 10^{-5}$ kPa^{-1} as the fully atomistic and CG simulation values, respectively, at $T = 500$ K. The description of other quantities, such as glass transition, and tacticity effects, are beyond the scope and the objectives of our current work.

Mixtures

The thermodynamic conditions of the polystyrene solutions studied here by molecular-dynamics simulations are summarised in Table 4. From these simulations we present first the results for PS + n-heptane. In Figure 12 we provide the temperature-volume fraction diagram for PS2030 + n-heptane, incorporating the experimental cloud curves given in Figure 1(b) of Reference [39]; the bounded regions of liquid-liquid demixing are indicated in the diagram by the grey shading. Volume fractions of the system are defined in relation to the relative values of the segment diameters σ; details are given in an *Appendix*, exemplified for the case of a PS4800 + n-heptane system. We note that alternative definitions based on the liquid-phase density have little impact on the results. This system is used to adjust the PS-heptane unlike interactions, through simulations at a composition of 24.3 mass% PS (corresponding to a volume fraction of $\Phi = 0.18$).

Simulations are carried out to examine states across a broad region of the phase diagram, indicated by the circles in Figure 12. Snapshots of equilibrium configurations that are rep-

Table 4: Details of systems simulated to study polystyrene solutions. N_{chain} and N_{sol} are the number of PS chains and solvent molecules, respectively. $\mathcal{N}_{\mathrm{tot}}$ is the total number of segments in the simulation box; mass% is the composition in mass-percent of PS, adjacent to which the corresponding volume fraction Φ is shown in parentheses. The bold numbers in the list of simulated temperatures correspond to those values where demixing is expected, in correspondence with Table 1.

System	N_{chain}	N_{sol}	$\mathcal{N}_{\mathrm{tot}}$	mass% (Φ)	T / K
PS2030 + n-heptane	160	19900	46200	14.0 (0.10)	**275**, 325, 400, 450, 500, **535**
PS2030 + n-heptane	347	21900	57680	24.3 (0.18)	**275**, 325, 400, 450, 500, **535**
PS2030 + n-heptane	480	15500	50200	38.5 (0.30)	**275**, 325, 400, 450, 500, **535**
PS4800 + n-heptane	294	42672	112392	24.8 (0.18)	**310**, 370, 420, 465, **530**
PS2030 + n-hexane	286	21248	53936	24.1 (0.18)	**280**, 330, 400, 450, **495**
PS4800 + n-hexane	215	36716	93212	24.6 (0.18)	**280, 340, 400, 495**
PS4800 + n-hexane	485	27316	99252	49.7 (0.40)	**280**, 400, **490**

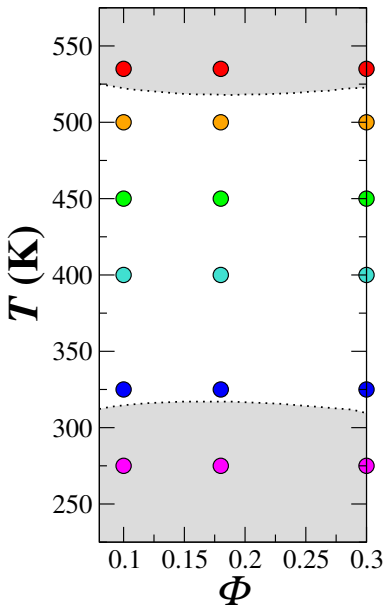

Figure 12: Temperature-volume fraction representation of the fluid-phase diagram for PS2030 + n-heptane. The dotted curves represent the experimental cloud curves obtained by Cowie and McEwen[39], bounding regions of liquid-liquid demixing, indicated by the grey shading. The circles correspond to the thermodynamic states studied in our current work.

resentative of these 18 states are presented in Figure 13. All of the snapshots presented in our work are produced using VMD[79,80]. We note that particular care is required in equilibrating the simulations corresponding to the higher-temperature states since the proximity of the critical point of n-heptane causes pronounced fluctuations in the system. Demixing can be easily observed in the snapshots for the extreme cases in temperature, in particular the lowest-temperature state $T = 275$ K, for all compositions. However, for intermediate temperatures, it is difficult to distinguish the condition of the mixture. To quantify the state (mixed/demixed) of the mixtures we follow the approach of Gelb and Müller[81]. Histograms of the local composition of the simulation box are collected. Initially, the box is divided into d_{cell}^3 subcells, where d_{cell} is adjusted for each system, depending on the composition, to produce the best possible noise-to-signal result. The total number n_{tot} of segments in each subcell as well as the segments n_{sol} corresponding only to solvent are accumulated in histograms of the $n_{\text{sol}}/n_{\text{tot}}$ ratio, fixing the width at 0.02 for all cases. This is repeated over hundreds of equilibrated configurations to provide good statistics. Finally, the frequency f for each $n_{\text{sol}}/n_{\text{tot}}$ is normalised with respect to the number of configurations and subcells, so that $\sum_i f_i = 1$. A symmetrical distribution centered around the global composition of $N_{\text{sol}}/N_{\text{tot}}$ indicates that, on average, the local compositions are similar throughout the system. By contrast, demixing is characterized by a bimodal distribution as its fingerprint, indicating how some subcells have a predominantly solvent-rich content, while others are mainly populated by PS segments.

The normalised distributions for each thermodynamic state are presented in Figures 14 (a) to (c). The vertical line indicates the overall system composition ratio $\mathcal{N}_{\text{sol}}/\mathcal{N}_{\text{tot}}$ (in terms of number of segments), for each simulation box. From Figure 14, at each composition, we can observe that the system at the lowest temperature of $T = 275$ K is characterized by a bimodal, highly asymmetrical distribution, indicating that $T = 275$ K corresponds to a demixed state. This is satisfying, given that $T = 275$ K is below the reported UCST (311 K)[39] for this system. At higher temperatures, the distribution gradually transforms

T/K	mass% = 14.0 ($\Phi = 0.10$)	mass% = 24.3 ($\Phi = 0.18$)	mass% = 38.5 ($\Phi = 0.30$)
535	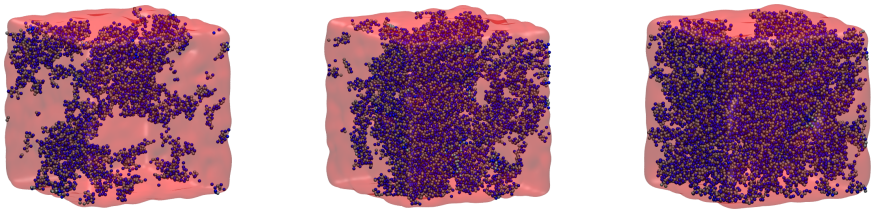		
500	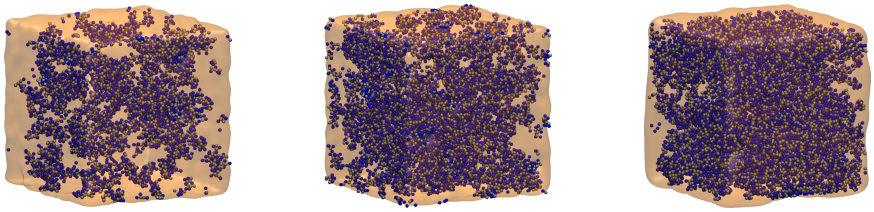		
450	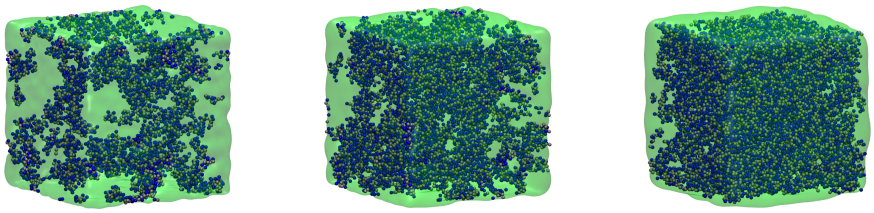		
400	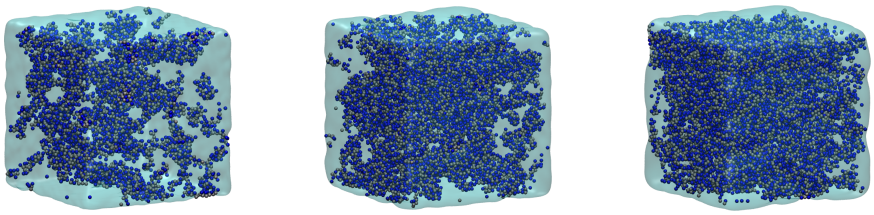		
325	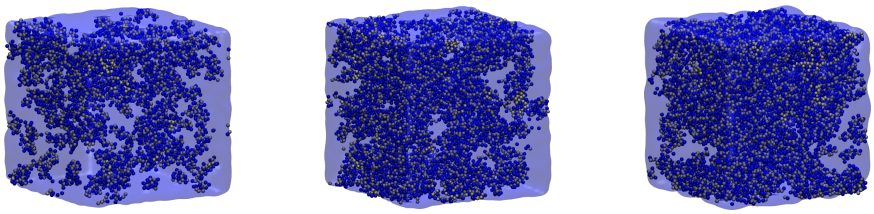		
275	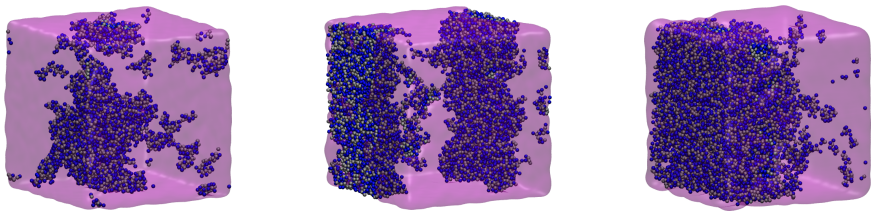		

Figure 13: Snapshots of equilibrated PS2030 + n-heptane at several temperatures and compositions. The thermodynamic states are colour-coded and correspond to those marked with small circles in the temperature-volume fraction phase diagram, *cf.* Figure 12. The solvent molecules are represented as a continuous transparent material to facilitate the visualisation.

into a symmetrical bell shape; this is particularly apparent for the systems at $T = 400$, 450, and 500 K. This behaviour is in agreement with the expectation from the fluid-phase diagram presented in Figure 12. At the highest temperature of $T = 535$ K the asymmetry appears again at each composition; this corresponds to a temperature above the reported LCST (515 K)[39] for this system. The histograms at $T = 325$ K exhibit an intermediate behaviour, which can be attributed to the proximity to the limiting UCST (see Figure 12). Exploratory evaluations of the Hsu *et al.*[21] model showed that it predicts the UCST at higher temperatures than the SAFT-γ model, inconsistent with the experimentally observed phase behaviour. This occurs despite slightly better predictions of the temperature-density behaviour by the Hsu *et al.*[21] model, suggesting an advantage of the top-down approach advocated here to describe phase separation.

We test the representability of the unlike-interaction parameters by exploring the behaviour of solutions comprising the longer polymer, PS4800. The results at the thermodynamic conditions indicated in Figure 15(a) correspond to the histogram distributions presented in Figure 15(b). In this case, the LCST is situated at a lower temperature of $T = 477$ K[39], so that our highest-temperature simulation is sufficiently above the LCST to capture the demixing expected in the high-temperature region. The histogram distributions for these systems are asymmetrical for the lowest and highest temperature, $T = 310$K and $T = 530$ K. On the other hand, the distribution is very symmetrical for the case of $T = 420$ K, while the distributions for $T = 370$ K and $T = 465$ K exhibit an intermediate behaviour, in agreement with the proximity of these thermodynamic states to the LCST and UCST limits observed experimentally by Cowie and McEwen[39].

The phase behaviour for PS + n-hexane is more challenging to reproduce since an "hourglass" phase diagram is expected in one of the systems but not in the other, as can be seen in Figures 16(a) and 17(a). The unlike-interaction parameters in this case are adjusted with simulations of the system PS2030 + n-hexane at a composition of mass% = 24.1, as described in our earlier section on *Unlike interactions for mixtures*. As for PS + n-heptane,

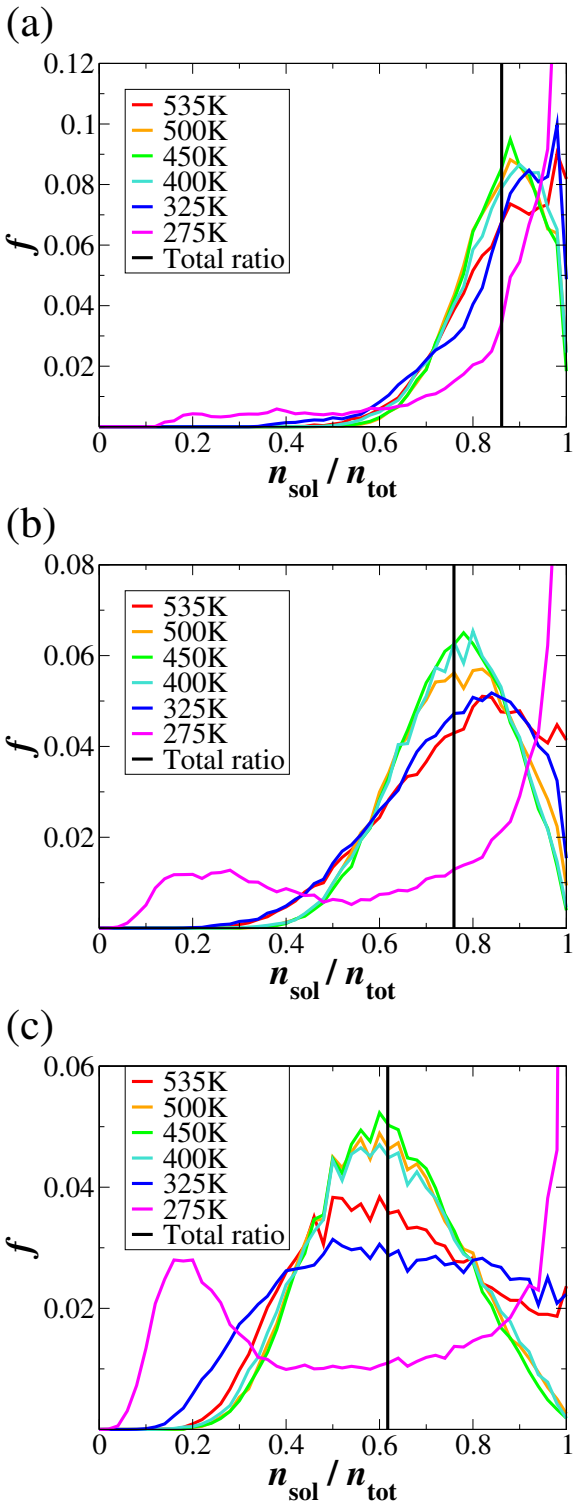

Figure 14: Normalised frequencies of the $n_{\rm sol}/n_{\rm tot}$ ratio for the system PS2030 + n-heptane, where $n_{\rm sol}$ is the number of solvent segments located in a system subcell and $n_{\rm tot}$ is the total number of segments, $n_{\rm tot} = n_{\rm sol} + n_{\rm PS}$, in the same subcell. (a) PS mass% = 14.0 ($\Phi = 0.10$), using $d^3_{\rm cell} = 125$ subcells; (b) PS mass% = 24.3 ($\Phi = 0.18$), using $d^3_{\rm cell} = 216$ subcells; (c) PS mass% = 38.5 ($\Phi = 0.30$), using $d^3_{\rm cell} = 343$ subcells. The vertical line indicates the overall system composition ratio $\mathcal{N}_{\rm sol}/\mathcal{N}_{\rm tot}$ (in terms of number of segments) for each simulation box.

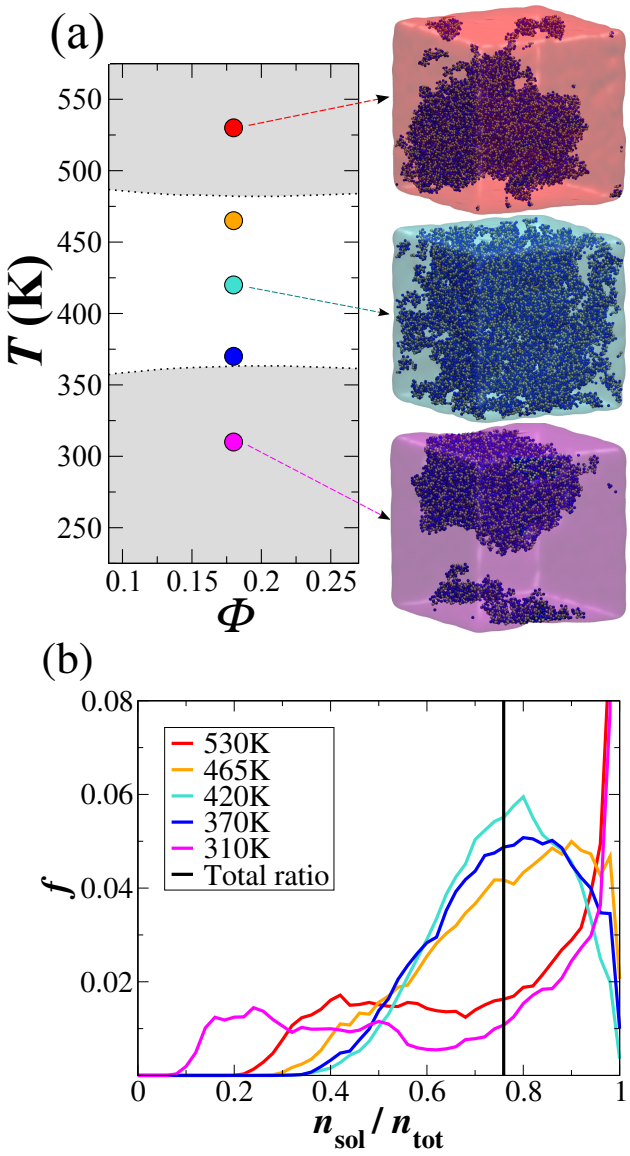

Figure 15: (a) Temperature-volume fraction phase diagram for PS4800 + n-heptane (*cf.* Figure 12). The snapshots of the simulation box represent equilibrium configurations of the system at T = 310, 420 and 535 K. (b) Normalised frequencies of the $n_{\mathrm{sol}}/n_{\mathrm{tot}}$ ratio (*cf.* Figure 14). The system composition is PS mass% = 24.8 (Φ = 0.18), and the histograms are calculated using $d^3_{\mathrm{cell}} = 216$ subcells.

simulations are carried out to examine the system across a broad region of the phase diagram; the thermodynamic states examined are indicated by the circles in Figure 16(a). The resulting composition distributions are shown in Figure 16(b). Again, the lowest- and highest-temperature states are characterized by asymmetrical bimodal distributions, indicating a demixed system. This can be appreciated from the snapshot of the configuration at the lowest temperature studied, $T = 310$ K, which corresponds to a state located far from the UCST. For this system, the practical upper limit of temperature for simulations is $T = 495$ K. Simulations at higher temperatures are not meaningful due to the fluctuations caused by the proximity of the critical temperature of n-hexane. The system at $T = 330$ K yields a histogram with similar asymmetry to the highest-temperature system. This behaviour is explained by the proximity of this state to the limiting UCST.

As a second test for the PS-hexane unlike-interaction parameters, the same force fields are used to simulate the PS4800 model. The experimental "hour-glass" phase diagram[39] and the thermodynamic states selected for simulation are depicted in Figure 17(a), including snapshots corresponding to the relevant equilibrium configurations. The local-composition histograms are shown in Figure 17 (b) and (c). The systems at the lower PS composition, mass% = 24.6 ($\Phi = 0.18$), exhibit asymmetrical distributions at all the simulated temperatures, as illustrated in Figure 17(b). The histograms for the higher PS composition, mass% = 49.7 ($\Phi = 0.40$), are represented in Figure 17(c). The states at $T = 280$ K and $T = 490$ K are characterized by very asymmetrical bimodal distributions, with strong peaks at low $n_{\mathrm{sol}}/n_{\mathrm{tol}}$ and at $n_{\mathrm{sol}}/n_{\mathrm{tol}} = 1$, indicative of liquid-liquid demixing. The state at $T = 400$ K, on the other hand, is characterized by a distribution that, although slightly asymmetrical, does not feature a second peak; this distribution resembles the bell shape indicative of complete miscibility corresponding to a single-phase system. It is particularly gratifying that, collectively, these results are entirely consistent with the "hour glass" phase diagram, illustrated in Figure 17(a), observed experimentally by Cowie and McEwen[39].

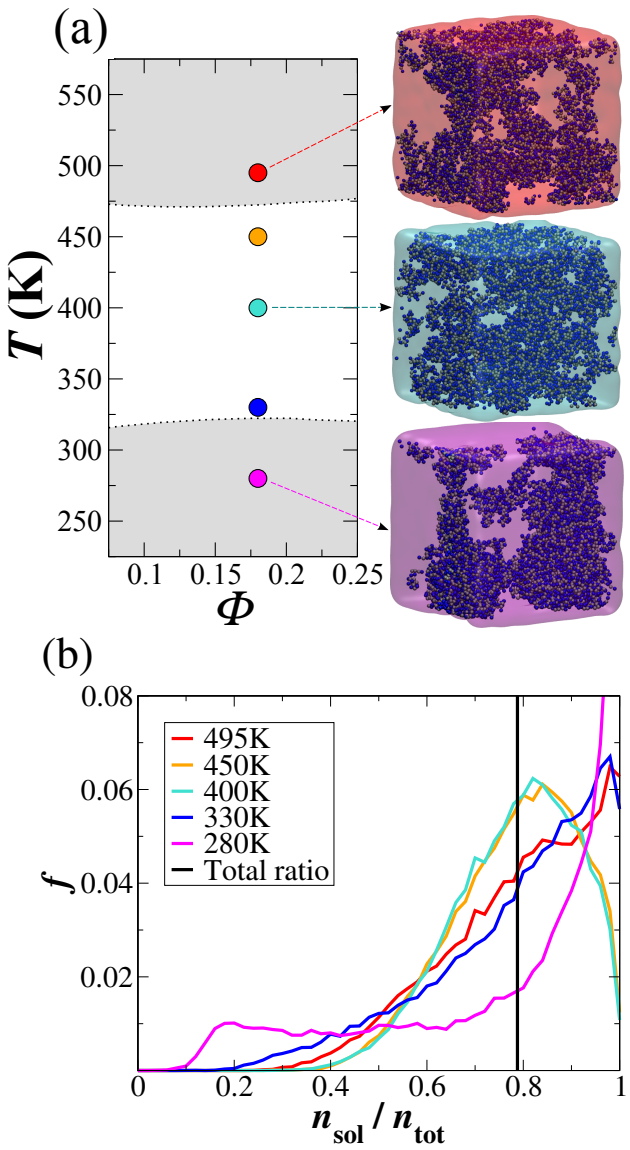

Figure 16: (a) Temperature-volume fraction phase diagram for PS2030 + n-hexane (*cf.* Figure 12). The snapshots of the simulation box represent equilibrium configurations of the system at $T = 280$, 400 and 495 K. (b) Normalised frequencies of the $n_{\mathrm{sol}}/n_{\mathrm{tot}}$ ratio (*cf.* Figure 14). The system composition is PS mass% = 24.1 ($\Phi = 0.18$), and the histograms are calculated using $d^3_{\mathrm{cell}} = 216$ subcells.

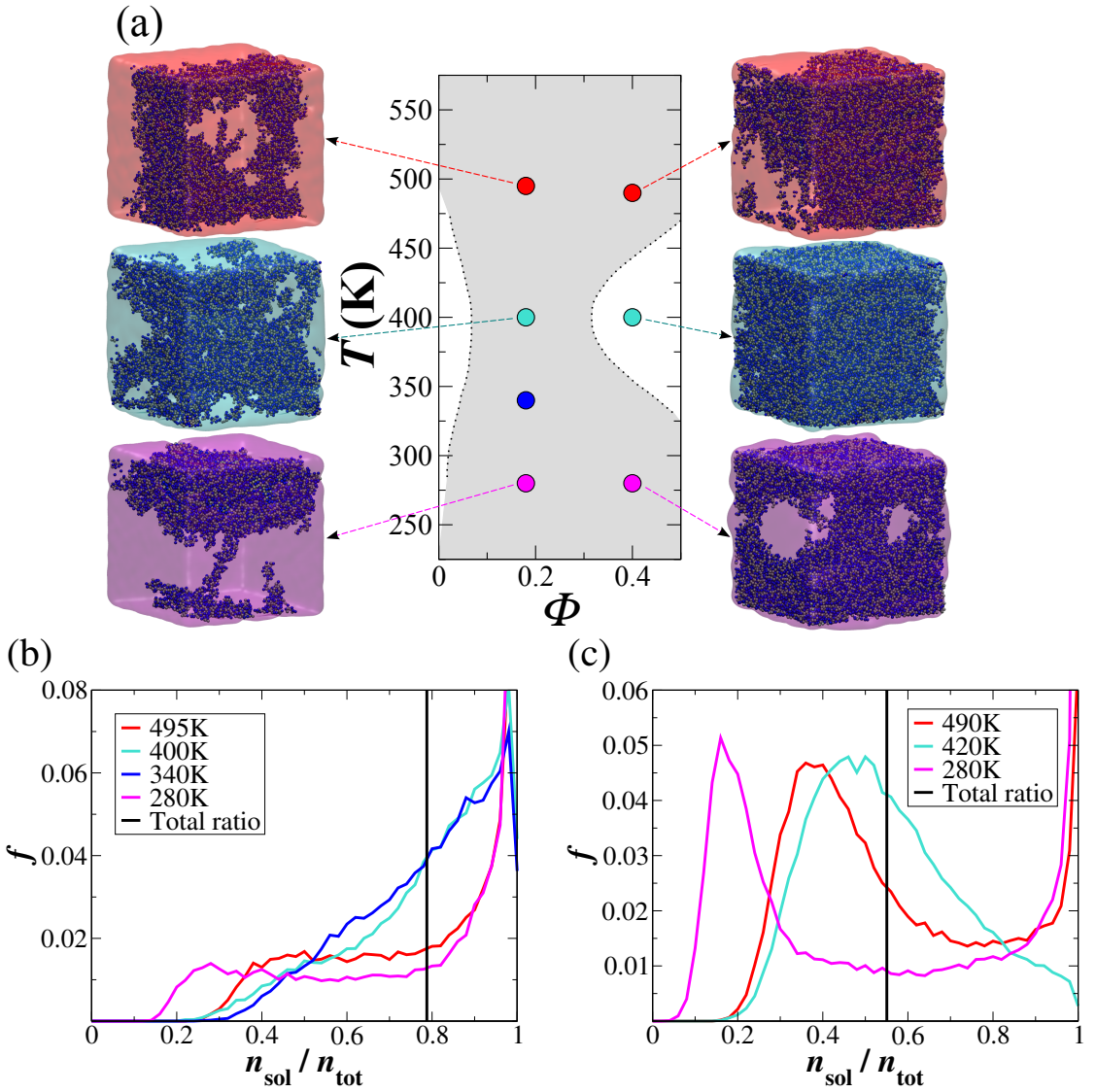

Figure 17: (a) Temperature-volume fraction phase diagram for PS4800 + n-hexane (*cf.* Figure 12). The snapshots of the simulation box represent equilibrium configurations of the system at different temperatures. (b) and (c) Normalised frequencies of the $n_{\mathrm{sol}}/n_{\mathrm{tot}}$ ratio (*cf.* Figure 14). The system compositions are PS mass% = 24.6 ($\Phi = 0.18$), and PS mass% = 49.7 ($\Phi = 0.40$). The histograms are calculated using $d^3_{\mathrm{cell}} = 216$ and $d^3_{\mathrm{cell}} = 343$ subcells, respectively.

Conclusions

We present a coarse-grained model for polystyrene and its solutions in aliphatic solvents, exemplified by *n*-hexane and *n*-heptane. The force-field parameters are obtained using the SAFT-γ Mie EoS[32,43]. This top-down approach is a simple way to generate CG models of long or complex molecules.

Systems of pure solvents are studied by MD simulations and theory, finding good agreement between the phase diagrams generated using both methodologies and those from experimental information. Melts of the PS models are tested under NPT and NVT conditions to study the effect of the polymer chain length, and of temperature and pressure. The quality of the results, in terms of density, end-to-end distance and radius of gyration, is similar to that obtained using other CG models reported in the literature for atactic polystyrene, generated via bottom-up procedures. Our CG polystyrene is simple enough to be used in simulations of large systems, such as those required to study PS in solution. At the same time, the description maintains the main features needed to provide good representability, *i.e.*, a reliable PS model that can be used under different thermodynamic conditions.

In the *Introduction* to our paper we alluded to the general issues of transferability (the ability to transfer a moiety (segment or bead) corresponding to a particular functional group in one molecule to another molecule containing the same functional group), representability (the ability of a model to represent the parent experimental system at different thermodynamic states), and robustness (the ability of a model to provide reliable descriptions across a wide range of different properties). We have demonstrated transferability of our CG PS model through the study of PS at significantly different molecular weights. We have also demonstrated representability of our models, through simulations both of pure-component and mixtures over broad regions of their respective phase diagrams. In this context we note, however, that the transferability of our mixture models to systems which are markedly different to those we have considered, and their representability at conditions differing very widely from those considered, have not been thoroughly tested. Any generalisation of the

assignment of the k_{ij} values to mixtures or conditions dramatically different to those considered in our current work should be performed with some care. One would expect the results to be very sensitive to the fine details of the values of the binary-interaction parameters. The fluid-phase behaviour showcased here is the result of a very fine balance between entropic and energetic contributions.

We have demonstrated the robustness of our models in terms of structural and thermodynamic properties. Since our models are not informed by atomistic simulations, they lack some inherent structural information. This, however, is not a limitation of the top-down approach. SAFT models can be "decorated" with appropriate intra-molecular interactions without compromising their accuracy in describing macroscopic properties.[48] This is particularly important in modelling transport properties such as diffusion and viscosity. An investigation of this in the context of our PS model was beyond the scope of our current study, and will form the basis of future work.

A natural extension of the present work in relation to mixtures involving PS, would be the exploration of more-complex systems. Simulation of multicomponent mixtures, over broader ranges of thermodynamic conditions, is an attractive possibility that would promote our understanding of the interplay of effects between the thermodynamic variables and the properties of the system for cases where the information is not accessible to experiment or theory.

Supporting information. Simulation details of solvents, PS melts, and PS-solvent mixtures. Plot of the PS-PS contribution to the system energy as a function of time.

The data underlying this article can be accessed on figshare at

`https://doi.org/10.6084/m9.figshare.3811572`

and used under the Creative Commons Attribution license.

Acknowledgments

We acknowledge the Skolkovo Foundation and BP for financial support through the UNI-HEAT project. Additional support to the Molecular Systems Engineering group from the Engineering and Physical Sciences Research Council (EPSRC) of the UK (research grants EP/E016340 and EP/J014958) and the Thomas Young Centre (TYC-101) is gratefully acknowledged. Simulations described herein were performed using the facilities of the Imperial College High Performance Computing Service.

References

(1) Mondello, M.; Yang, H.-J.; Furuya, H.; Roe, R.-J. Molecular dynamics simulation of atactic polystyrene. 1. Comparison with X-ray scattering data. *Macromolecules* **1994**, *27*, 3566–3574.

(2) Karanikas, S.; Economou, I. G. Molecular simulation of structure, thermodynamic and transport properties of polyacrylonitrile, polystyrene and their alternating copolymers in high temperatures. *Eur. Polym. J.* **2011**, *47*, 735–745.

(3) Lazutin, A. A.; Glagolev, M. K.; Vasilevskaya, V. V.; Khoklov, A. R. Hypercrosslinked polystyrene networks: An atomistic molecular dynamics simulation combined with a mapping/reverse mapping procedure. *J. Chem. Phys.* **2014**, *140*, 134903.

(4) Cuthbert, T. R.; Wagner, N. J.; Paulaitis, M. E. Molecular simulation of glassy polystyrene: Size effects on gas solubilities. *Macromolecules* **1997**, *30*, 3058–3065.

(5) Yang, F.; Ghosh, S.; Lee, L. J. Molecular dynamics simulation based size and rate dependent constitutive model of polystyrene thin films. *Comput. Mech.* **2012**, *50*, 169–184.

(6) Ndoro, T. V.; Voyiatzis, E.; Ghanbari, A.; Theodorou, D. N.; Böhm, M. C.; Müller-Plathe, F. Interface of grafted and ungrafted silica nanoparticles with a polystyrene matrix: Atomistic molecular dynamics simulations. *Macromolecules* **2011**, *44*, 2316–2327.

(7) Marcon, V.; van der Vegt, N. F. How does low-molecular-weight polystyrene dissolve: osmotic swelling *vs.* surface dissolution. *Soft matter* **2014**, *10*, 9059–9064.

(8) Müller, E. A.; Jackson, G. Force-field parameters from the SAFT-γ equation of state for use in coarse-grained molecular simulations. *Ann. Rev. Chem. Biomol. Eng.* **2014**, *5*, 405–427.

(9) Karimi-Varzaneh, H. A.; van der Vegt, N. F.; Müller-Plathe, F.; Carbone, P. How good are coarse-grained polymer models? A comparison for atactic polystyrene. *ChemPhysChem.* **2012**, *13*, 3428–3439.

(10) Milano, G.; Müller-Plathe, F. Mapping atomistic simulations to mesoscopic models: A systematic coarse-graining procedure for vinyl polymer chains. *J. Phys. Chem. B* **2005**, *109*, 18609–18619.

(11) Sun, Q.; Faller, R. Crossover from unentangled to entangled dynamics in a systematically coarse-grained polystyrene melt. *Macromolecules* **2006**, *39*, 812–820.

(12) Sun, Q.; Pon, F. R.; Faller, R. Multiscale modeling of polystyrene in various environments. *Fluid Phase Equilib.* **2007**, *261*, 35–40.

(13) Sun, Q.; Faller, R. Phase separation in polyisoprene/polystyrene blends by a systematically coarse-grained model. *J. Chem. Phys.* **2007**, *126*, 144908.

(14) Bayramoglu, B.; Faller, R. Coarse-grained modeling of polystyrene in various environments by iterative Boltzmann inversion. *Macromolecules* **2012**, *45*, 9205–9219.

(15) Rossi, G.; Monticelli, L.; Puisto, S. R.; Vattulainen, I.; Ala-Nissila, T. Coarse-graining polymers with the MARTINI force-field: Polystyrene as a benchmark case. *Soft Matter* **2011**, *7*, 698–708.

(16) Harmandaris, V.; Adhikari, N.; van der Vegt, N. F.; Kremer, K. Hierarchical modeling of polystyrene: From atomistic to coarse-grained simulations. *Macromolecules* **2006**, *39*, 6708–6719.

(17) Harmandaris, V. A.; Kremer, K. Dynamics of polystyrene melts through hierarchical multiscale simulations. *Macromolecules* **2009**, *42*, 791–802.

(18) Harmandaris, V. A.; Reith, D.; Van der Vegt, N. F.; Kremer, K. Comparison between

coarse-graining models for polymer systems: Two mapping schemes for polystyrene. *Macromol. Chem. Phys.* **2007**, *208*, 2109–2120.

(19) Fritz, D.; Harmandaris, V. A.; Kremer, K.; van der Vegt, N. F. Coarse-grained polymer melts based on isolated atomistic chains: Simulation of polystyrene of different tacticities. *Macromolecules* **2009**, *42*, 7579–7588.

(20) Qian, H.-J.; Carbone, P.; Chen, X.; Karimi-Varzaneh, H. A.; Liew, C. C.; Müller-Plathe, F. Temperature-transferable coarse-grained potentials for ethylbenzene, polystyrene, and their mixtures. *Macromolecules* **2008**, *41*, 9919–9929.

(21) Hsu, D. D.; Xia, W.; Arturo, S. G.; Keten, S. Thermomechanically consistent and temperature transferable coarse-graining of atactic polystyrene. *Macromolecules* **2015**, *48*, 3057–3068.

(22) Rao, S.; Li, X.; Liang, H. Developing coarse-grained force fields for polystyrene with different chain lengths from atomistic simulation. *Macromol. Res.* **2007**, *15*, 610–616.

(23) Spyriouni, T.; Tzoumanekas, C.; Theodorou, D.; Müller-Plathe, F.; Milano, G. Coarse-grained and reverse-mapped united-atom simulations of long-chain atactic polystyrene melts: Structure, thermodynamic properties, chain conformation, and entanglements. *Macromolecules* **2007**, *40*, 3876–3885.

(24) Agrawal, A.; Aryal, D.; Perahia, D.; Ge, T.; Grest, G. S. Coarse-graining atactic polystyrene and its analogues. *Macromolecules* **2014**, *47*, 3210–3218.

(25) Rosch, T. W.; Brennan, J. K.; Izvekov, S.; Andzelm, J. W. Exploring the ability of a multiscale coarse-grained potential to describe the stress-strain response of glassy polystyrene. *Phys. Rev. E* **2013**, *87*, 042606.

(26) Wu, C. Phase morphologies of binary polymer blends predicted by systematically coarse-grained models. *Macromol. Theor. Simul.* **2016**, DOI:0.1002/mats.201500087.

(27) Carbone, P.; Varzaneh, H. A. K.; Chen, X.; Müller-Plathe, F. Transferability of coarse-grained force fields: The polymer case. *J. Chem. Phys.* **2008**, *128*, 064904.

(28) Papaioannou, V.; Lafitte, T.; Avendaño, C.; Adjiman, C. S.; Jackson, G.; Müller, E. A.; Galindo, A. Group contribution methodology based on the statistical associating fluid theory for heteronuclear molecules formed from Mie segments. *J. Chem. Phys.* **2014**, *140*, 054107.

(29) Chapman, W. G.; Gubbins, K. E.; Jackson, G.; Radosz, M. SAFT: Equation-of-state solution model for associating fluids. *Fluid Phase Equilib.* **1989**, *52*, 31–38.

(30) Chapman, W. G.; Gubbins, K. E.; Jackson, G.; Radosz, M. New reference equation of state for associating liquids. *Ind. Eng. Chem. Res.* **1990**, *29*, 1709–1721.

(31) Kontogeorgis, G. M.; Folas, G. K. *Thermodynamic models for industrial applications: From classical and advanced mixing rules to association theories*; Wiley: Chichester, UK, 2010.

(32) Lafitte, T.; Apostolakou, A.; Avendaño, C.; Galindo, A.; Adjiman, C. S.; Müller, E. A.; Jackson, G. Accurate statistical associating fluid theory for chain molecules formed from Mie segments. *J. Chem. Phys.* **2013**, *139*, 154504.

(33) Avendaño, C.; Lafitte, T.; Galindo, A.; Adjiman, C. S.; Jackson, G.; Müller, E. A. SAFT-γ force field for the simulation of molecular fluids. 1. A single-site coarse grained model of carbon dioxide. *J. Phys. Chem. B* **2011**, *115*, 11154–11169.

(34) Avendaño, C.; Lafitte, T.; Adjiman, C. S.; Galindo, A.; Müller, E. A.; Jackson, G. SAFT-γ force field for the simulation of molecular fluids: 2. Coarse-grained models of greenhouse gases, refrigerants, and long alkanes. *J. Phys. Chem. B* **2013**, *117*, 2717–2733.

(35) Imre, A.; Van Hook, W. A. Liquid–liquid demixing from solutions of polystyrene. 1. A review. 2. Improved correlation with solvent properties. *J. Phys. Chem. Ref. Dat.* **1996**, *25*, 637–661.

(36) Koningsveld, R.; Stockmayer, W. H.; Nies, E. *Polymer phase diagrams: a textbook*; Oxford University Press: Oxford, UK, 2001.

(37) Paricaud, P.; Galindo, A.; Jackson, G. Understanding liquid-liquid immiscibility and LCST behaviour in polymer solutions with a Wertheim TPT1 description. *Mol. Phys.* **2003**, *101*, 2575–2600.

(38) Kao, H.-H.; Jackson, G.; Trusler, J. P. M.; Higgins, J. S. Global pressure-temperature fluid-phase equilibria of solutions of polystyrene in hydrocarbons. *Mol. Phys.* **2017**, In preparation.

(39) Cowie, J.; McEwen, I. Polymer-cosolvent systems: 5. Upper and lower critical solution temperatures of polystyrene in n-alkanes. *Polymer* **1983**, *24*, 1445–1448.

(40) Ramrattan, N.; Avendaño, C.; Müller, E.; Galindo, A. A corresponding-states framework for the description of the Mie family of intermolecular potentials. *Mol. Phys.* **2015**, 1–16.

(41) London, F. The general theory of molecular forces. *Trans. Faraday Soc.* **1937**, *33*, 8b–26.

(42) Dufal, S.; Lafitte, T.; Galindo, A.; Jackson, G.; Haslam, A. J. Developing intermolecular-potential models for use with the SAFT-VR Mie equation of state. *AIChE J.* **2015**, *61*, 2891–2912.

(43) Mejía, A.; Herdes, C.; Müller, E. A. Force fields for coarse-grained molecular simulations from a corresponding states correlation. *Industrial & Engineering Chemistry Research*

2014, *53*, 4131–4141, the procedure outlined in this manuscript is employed to present parameters for $>$ 5000 compounds (see Ref. [45]).

(44) Herdes, C.; Totton, T. S.; Müller, E. A. Coarse grained force field for the molecular simulation of natural gases and condensates. *Fluid Phase Equilib.* **2015**, *406*, 91–100.

(45) Ervik, Å.; Mejía, A.; Müller, E. A. Bottled SAFT: a web app providing SAFT-γ Mie force field parameters for thousands of molecular fluids. *J. Chem. Info. Model.* **2016**, DOI:10.1021/acs.jcim.6b00149.

(46) Lymperiadis, A.; Adjiman, C. S.; Galindo, A.; Jackson, G. A group contribution method for associating chain molecules based on the statistical associating fluid theory (SAFT-γ). *J. Chem. Phys.* **2007**, *127*, 234903.

(47) Lafitte, T.; Avendaño, C.; Papaioannou, V.; Galindo, A.; Adjiman, C. S.; Jackson, G.; Müller, E. A. SAFT-γ force field for the simulation of molecular fluids: 3. Coarse-grained models of benzene and hetero-group models of n-decylbenzene. *Mol. Phys.* **2012**, *110*, 1189–1203.

(48) Rahman, S.; Lobanova, O.; Braga, C.; Raptis, V.; Avendaño, C.; Müller, E. A.; Jackson, G.; Galindo, A. SAFT-γ force field for the simulation of molecular fluids. 5. Hetero-group coarse grained models of linear alkanes and the importance of intra-molecular interactions. **2017**, In preparation.

(49) Theodorakis, P. E.; Müller, E. A.; Craster, R. V.; Matar, O. K. Superspreading: Mechanisms and molecular design. *Langmuir* **2015**, *31*, 2304–2309.

(50) Herdes, C.; Santiso, E. E.; James, C.; Eastoe, J.; Müller, E. A. Modelling the interfacial behaviour of dilute light-switching surfactant solutions. *J. Colloid Interface Sci.* **2015**, *445*, 16–23.

(51) Morgado, P.; Lobanova, O.; Müller, E. A.; Jackson, G.; Almeida, M.; Filipe, E. J. M. SAFT-γ force field for the simulation of molecular fluids: 8. Hetero-segmented coarse-grained models of perfluoroalkylalkanes assessed with new vapour–liquid interfacial tension data. *Mol. Phys.* **2016**, 1–18.

(52) Haslam, A. J.; Galindo, A.; Jackson, G. Prediction of binary intermolecular potential parameters for use in modelling fluid mixtures. *Fluid Phase Equilib.* **2008**, *266*, 105–128.

(53) Kao, H.-H. Understanding the fluid phase equilibria and polydispersity in polymer systems. Ph.D. thesis, Imperial College London, 2009.

(54) Dufal, S.; Papaioannou, V.; Sadeqzadeh, M.; Pogiatzis, T.; Chremos, A.; Adjiman, C. S.; Jackson, G.; Galindo, A. Prediction of thermodynamic properties and phase behavior of fluids and mixtures with the SAFT-γ Mie group-contribution equation of state. *Journal of Chemical & Engineering Data* **2014**, *59*, 3272–3288.

(55) Jover, J.; Galindo, A.; Jackson, G.; Müller, E. A.; Haslam, A. J. Fluid–fluid coexistence in an athermal colloid–polymer mixture: Thermodynamic perturbation theory and continuum molecular-dynamics simulation. *Mol. Phys.* **2015**, *113*, 2608–2628.

(56) Lobanova, O.; Mejía, A.; Jackson, G.; Müller, E. A. SAFT-γ force field for the simulation of molecular fluids 6: Binary and ternary mixtures comprising water, carbon dioxide, and n-alkanes. *J. Chem. Thermodyn.* **2016**, *93*, 320–336.

(57) HOOMD-blue. `http://codeblue.umich.edu/hoomd-blue`.

(58) Anderson, J. A.; Lorenz, C. D.; Travesset, A. General purpose molecular dynamics simulations fully implemented on graphics processing units. *J. Comput. Phys.* **2008**, *227*, 5342–5359.

(59) Glaser, J.; Nguyen, T. D.; Anderson, J. A.; Lui, P.; Spiga, F.; Millan, J. A.; Morse, D. C.; Glotzer, S. C. Strong scaling of general-purpose molecular dynamics simulations on GPUs. *Computer Physics Communications* **2015**, *192*, 97–107.

(60) Martyna, G. J.; Tobias, D. J.; Klein, M. L. Constant pressure molecular dynamics algorithms. *J. Chem. Phys.* **1994**, *101*, 4177–4189.

(61) Cao, J.; Martyna, G. Adiabatic path integral molecular dynamics methods. II. Algorithms. *J. Chem. Phys.* **1996**, *104*, 2028–2035.

(62) Nosé, S. A unified formulation of the constant temperature molecular dynamics methods. *J. Chem. Phys.* **1984**, *81*, 511–519.

(63) Hoover, W. G. Canonical dynamics: Equilibrium phase-space distributions. *Phys. Rev. A* **1985**, *31*, 1695.

(64) Tuckerman, M. E.; Alejandre, J.; López-Rendón, R.; Jochim, A. L.; Martyna, G. J. A Liouville-operator derived measure-preserving integrator for molecular dynamics simulations in the isothermal–isobaric ensemble. *J. Phys. A: Math Gen* **2006**, *39*, 5629.

(65) Yu, T.-Q.; Alejandre, J.; López-Rendón, R.; Martyna, G. J.; Tuckerman, M. E. Measure-preserving integrators for molecular dynamics in the isothermal–isobaric ensemble derived from the Liouville operator. *Chemical Physics* **2010**, *370*, 294–305.

(66) Manion, J. A.; Huie, R. E.; Levin, R. D.; Burgess Jr, D. R.; Orkin, V. L.; Tsang, W.; McGivern, W. S.; Hudgens, J. W.; Knyazev, V. D.; Atkinson, D. B.; Others, NIST Chemical Kinetics Database. `http://kinetics.nist.gov`, NIST Standard Reference Database 17, Version 7.0 (Web Version), Release 1.6. 8, Data version 2013.03, National Institute of Standards and Technology, Gaithersburg, Maryland, 20899–8320.

(67) Polt, A.; Platzer, B.; Maurer, G. Parameter der thermischen Zustandsgleichung von Bender fuer 14 mehratomige reine Stoffe. *Chem. Tech.(Leipzig)* **1992**, *44*, 216–224.

(68) Trokhymchuk, A.; Alejandre, J. Computer simulations of liquid/vapor interface in Lennard-Jones fluids: Some questions and answers. *J. Chem. Phys.* **1999**, *111*, 8510–8523.

(69) Martínez-Veracoechea, F.; Müller, E. Temperature-quench molecular dynamics simulations for fluid phase equilibria. *Mol. Simul.* **2005**, *31*, 33–43.

(70) Van Der Spoel, D.; Lindahl, E.; Hess, B.; Groenhof, G.; Mark, A. E.; Berendsen, H. J. GROMACS: fast, flexible, and free. *J. Comput. Chem.* **2005**, *26*, 1701–1718.

(71) Walsh, D.; Zoller, P. *Standard pressure volume temperature data for polymers*; CRC Press: Boca Raton, USA, 1995.

(72) Cotton, J.; Decker, D.; Benoit, H.; Farnoux, B.; Higgins, J.; Jannink, G.; Ober, R.; Picot, C.; Des Cloizeaux, J. Conformation of polymer chain in the bulk. *Macromolecules* **1974**, *7*, 863–872.

(73) Yoon, D.; Flory, P. Small-angle X-ray and neutron scattering by polymethylene, polyoxyethylene, and polystyrene chains. *Macromolecules* **1976**, *9*, 294–299.

(74) Mark, J.; Ngai, K.; Graessley, W.; Mandelkern, L.; Samulski, E.; Koenig, J.; Wignall, G. *Physical properties of polymers (3rd ed.)*; Cambridge University Press: Cambridge, UK, 2004.

(75) Green, P. F.; Palmstrom, C. J.; Mayer, J. W.; Kramer, E. J. Marker displacement measurements of polymer-polymer interdiffusion. *Macromolecules* **1985**, *18*, 501–507.

(76) Antonietti, M.; Coutandin, J.; Sillescu, H. Diffusion of linear polystyrene molecules in matrixes of different molecular weights. *Macromolecules* **1986**, *19*, 793–798.

(77) Antonietti, M.; Fölsch, K. J.; Sillescu, H. Critical chain lengths in polystyrene bulk diffusion. *Macromol. Chem. Phys.* **1987**, *188*, 2317–2324.

(78) Bachus, R.; Kimmich, R. Molecular weight and temperature dependence of self-diffusion coefficients in polyethylene and polystyrene melts investigated using a modified NMR field-gradient technique. *Polymer* **1983**, *24*, 964–970.

(79) Humphrey, W.; Dalke, A.; Schulten, K. VMD: visual molecular dynamics. *J. Mol. Graphics* **1996**, *14*, 33–38.

(80) Stone, J. E. An efficient library for parallel ray tracing and animation. M.Sc. thesis, Univeristy of Missouri-Rolla, 1998.

(81) Gelb, L. D.; Müller, E. A. Location of phase equilibria by temperature-quench molecular dynamics simulations. *Fluid Phase Equilib.* **2002**, *203*, 1–14.

Appendix: Volume fractions

The volume fractions of our systems are defined in terms of the segment diameters as

$$\Phi = \frac{N_{\text{chain}} N_{\text{mono}} \left(\sigma_{\text{bbn}}^3 + \sigma_{\text{bch}}^3 \right)}{N_{\text{chain}} N_{\text{mono}} \left(\sigma_{\text{bbn}}^3 + \sigma_{\text{bch}}^3 \right) + 2 N_{\text{sol}} \sigma_{\text{sol}}^3}, \tag{7}$$

where N_{chain} is the number of PS chains, N_{mono} is the number of styrene units, and σ is the backbone (bbn), branch (bch), or solvent (sol) diameter. This definition is exact for hard (athermal) systems, but not for soft spheres. We recognise that a more general volume-fraction definition,

$$\Phi = \frac{V_{\text{PS}}}{V_{\text{PS}} + V_{\text{sol}}}, \tag{8}$$

can be written in terms of densities:

$$\Phi = \frac{m_{\text{PS}} \rho_{\text{PS}}}{m_{\text{PS}} \rho_{\text{sol}} + m_{\text{sol}} \rho_{\text{PS}}}, \tag{9}$$

but note that this last definition relies on the knowledge of the temperature-dependent densities, hence is impractical. Numerically, however, both definitions produce similar results. As an example, the PS4800 + heptane system has a fixed volume fraction of $\Phi = 0.18$ following Equation 7. To calculate the corresponding values through Equation 9, we use the temperature-dependent PS densities obtained with the pure melt simulations, $N_{\text{mono}} = 10$ system, and the densities of pure heptane. The resulting values range from 0.17 to 0.16 for temperatures between 310 K and 465 K, while only the highest-temperature system, at 530 K, has a volume fraction that deviates from the fixed value by more than 25%, with a volume fraction of $\Phi = 0.13$.

For Table of Contents use only

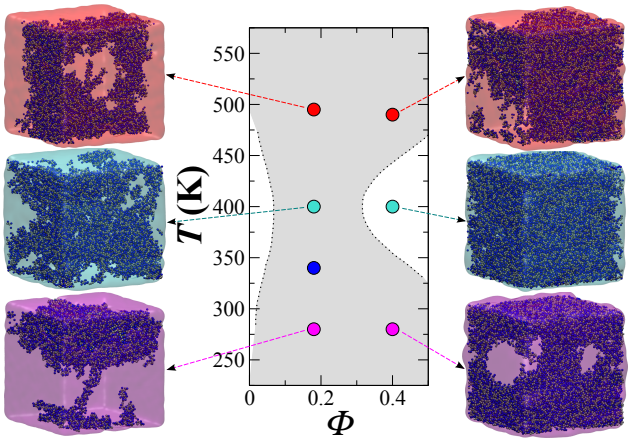

Group-contribution coarse-grained molecular simulations of polystyrene melts and polystyrene solutions in alkanes using SAFT-γ force fields

Guadalupe Jiménez-Serratos

Carmelo Herdes

Andrew J. Haslam

George Jackson

Erich A. Müller